Dynamics of cylindrical domain walls in smectic C liquid crystals

2009 J. Phys. A: Math. Theor. 42 235501

(http://iopscience.iop.org/1751-8121/42/23/235501)

IOP PUBLISHING JOURNAL OF PHYSICS A: MATHEMATICAL AND THEORETICAL

J. Phys. A: Math. Theor. **42** (2009) 235501 (26pp) doi:10.1088/1751-8113/42/23/235501

Dynamics of cylindrical domain walls in smectic C liquid crystals

I W Stewart and E J Wigham

Department of Mathematics, University of Strathclyde, Livingstone Tower, 26 Richmond Street, Glasgow, G1 1XH, UK

E-mail: i.w.stewart@strath.ac.uk

Received 3 February 2009, in final form 6 April 2009
Published 15 May 2009
Online at stacks.iop.org/JPhysA/42/235501

Abstract

An analysis of the dynamics of cylindrical domain walls in planar aligned samples of smectic C liquid crystals is presented. A circular magnetic field, induced by an electric current, drives a time-dependent reorientation of the corresponding radially dependent director field. Nonlinear approximations to the relevant nonlinear dynamic equation, derived from smectic continuum theory, are solved in a comoving coordinated frame: exact solutions are found for a π-wall and numerical solutions are calculated for $\frac{\pi}{2}$-walls. Each calculation begins with an assumed initial state for the director that is a prescribed cylindrical domain wall. Such an initial wall will proceed to expand or contract as its central core propagates radially inwards or outwards, depending on the boundary conditions for the director, the elastic constants, the magnitude of the field and the sign of the magnetic anisotropy of the liquid crystal.

PACS numbers: 61.30.−v, 61.30.Dk

1. Introduction

Liquid crystals are anisotropic fluids that generally consist of elongated rod-like molecules which have a preferred local average direction. This direction is commonly described by the unit vector **n**, usually called the director. Smectic liquid crystals are layered structures in which **n** makes an angle θ with respect to the local smectic layer normal **a**, as shown in figure 1. Although the angle θ, also known as the smectic cone angle, is usually temperature dependent, it may, nevertheless, vary because of competition between boundary conditions, elastic effects and smectic layer compressional effects. The idealized smectic A (SmA) liquid crystal phase is said to occur when $\theta \equiv 0$, in which case **n** and **a** coincide. When $\theta \neq 0$ the structure is called a smectic C (SmC) liquid crystal. In the isothermal SmC phase it is generally acceptable to assume that θ remains at a fixed constant angle so that the director **n** is

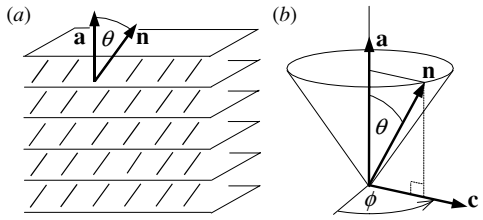

Figure 1. (*a*) The local layer alignment in SmC liquid crystals. The short bold lines represent the molecular alignment, denoted by the director **n**, within parallel layers. The director is tilted at an angle θ relative to the local layer normal **a**. (*b*) The director **n** is constrained to lie on the surface of a fictitious cone when $\theta \neq 0$ is fixed; the vector **c** is the unit orthogonal projection of **n** onto the smectic planes. The orientation of **n** is fully described by **a** and the angle ϕ that **c** makes measured relative to some fixed axis within the smectic planes.

constrained to lie on the surface of a fictitious cone, as indicated in figure 1(*b*); it often proves convenient to introduce the unit orthogonal projection of **n** onto the smectic planes, denoted by **c**. In general, the orientation of **n** can be completely described by **a** and **c** because

$$\mathbf{n} = \mathbf{a}\cos\theta + \mathbf{c}\sin\theta. \tag{1.1}$$

The orientation angle ϕ of **c**, measured relative to some fixed axis within the smectic planes, is often introduced in mathematical descriptions of SmC. If the smectic layers and the smectic cone angle θ remain fixed, as will be the case here when **a** is a constant vector, then the orientation of the director within the smectic layers is completely described by means of the angle ϕ via (1.1). More general details on the physical and mathematical descriptions of liquid crystals can be found in the books by de Gennes and Prost [1], Chandrasekhar [2] and Stewart [3].

The alignment of the director **n** is known to be affected by applied magnetic fields. Isothermal conditions will be supposed throughout this paper so that the orientation of **n** is completely described by the orientation of **c**, as described above. For liquid crystals, **n** prefers to align parallel to the field when the magnetic anisotropy $\Delta\chi$ is positive and perpendicular to the field when $\Delta\chi$ is negative. Moreover, this alignment can also depend upon bulk elastic effects due to elastic distortions of the director. The distortions of **n** that arise from elasticity and applied fields are characterized via elastic and magnetic energy densities and these are introduced below in section 2. The imposition of boundary conditions on **n** creates a competition between the effects of elasticity and applied magnetic fields that will depend on the magnitudes of the bulk elastic constants and the field. When additional initial conditions are prescribed then this competition will lead to a time-dependent director profile that requires a dynamic theory for its description: the dynamic theory for SmC liquid crystals is also outlined in section 2. More general details on the elastic and magnetic properties of liquid crystals can be found in [1–3].

The problem to be discussed in this paper concerns the radial propagation of a circular domain wall in planar aligned SmC samples. A circular magnetic field, induced by an electric current passing along a straight wire, may produce an annular domain wall when the magnetic field direction and boundary conditions encourage a director alignment near the wire and radially far from the wire that conflicts with the elastic preferences for distortions of the director in the bulk, as will be described below. Supplying initial conditions will result in the radial propagation of this domain wall and it is this effect, and its consequences, that will be investigated here. Radially propagating domain walls in nematics have been discussed by

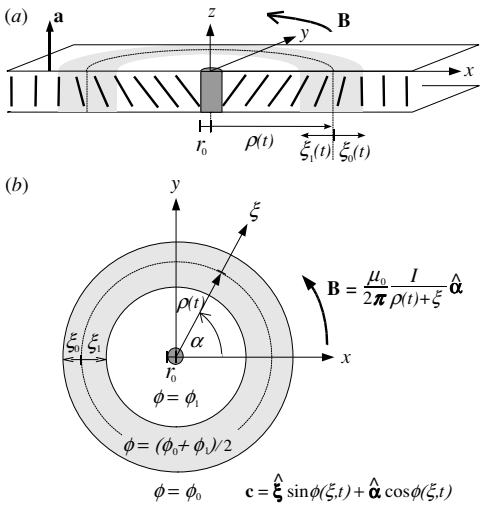

Figure 2. (*a*) Cross-section in the xz-plane showing a representative SmC layer. Bold lines represent the director alignment as seen by an observer looking along the y-axis. A wire of radius r_0 carries a current that induces a circular magnetic induction **B**. The smectic layer normal is **a**. The domain wall occurs in the annular grey region over which the director reorients between two constant states. The central core of the wall is located at $\rho(t)$. The distances $\xi_0(t)$ and $\xi_1(t)$ are the 'outer' and 'inner' wall half-widths, respectively. (*b*) The geometry as seen by an observer looking down the z-axis. The orientation of **c** is described via the angle $\phi(\xi, t)$; ϕ_0 and ϕ_1 are the constant orientation angles of **c** in those parts of the sample in the outer and inner regions, respectively, that are exterior to the wall, as defined in (2.5). At the core of the wall $\phi = (\phi_0 + \phi_1)/2$.

Stelzer and Arodź [4] and Arodź and Larsen [5] and these articles have motivated much of the investigation here. It should also be mentioned that computer simulations of domain wall growth in ferroelectric smectic C (SmC*) liquid crystals have been reported by Maclennan *et al* [6] who introduced a schematic figure of a radially symmetric domain wall and corresponding wall width which are very similar in nature to those presented in figure 2(*b*) in the context of smectic liquid crystals. Rotation of the vector **c** through the angle π has been observed experimentally by Pociecha *et al* [7] in free standing films of SmC. The π-walls observed in [7] were static and did require some change in the smectic layer thickness when labyrinth structures developed. The π-walls described below in section 3.2 are idealized versions of annular π-walls which, unlike the experiments considered in [7], may also propagate due to the presence of an induced magnetic field that encourages a competition between competing constant equilibrium orientation angles for the director. Comments on cylindrical annular geometries and possible orientations of the director in nematics have been made by Palffy-Muhoray *et al* [8]; in the context of SmC, these are especially relevant in relation to the region around the centre of the sample introduced below. The behaviour of the director in the vicinity of line defects or polymer fibres, and also in the interior of confining cavities, leads to the study of liquid crystals around an effectively isotropic internal cylinder [8], such as the aforementioned wire in the set-up mentioned above for SmC.

Section 2.1 introduces the geometrical set-up for the problem and a more detailed mathematical model of the structure of the domain wall described in a comoving coordinate frame. Section 2.2 briefly introduces SmC liquid crystal dynamic theory, while section 2.3 derives the nonlinear governing dynamic equation (2.40) that will be the basis of our analysis.

Given the highly nonlinear form of this equation, a polynomial expansion will be derived in section 3.1 that will allow nonlinear approximating equations to be made which can be solved exactly for the case of a π-wall in section 3.2. This approach has been motivated by a series of articles on thick domain walls and related types of radially symmetric domain walls in nematic liquid crystals studied by Arodź [9, 10], Arodź and Stelzer [11], Stelzer and Arodź [4] and Arodź and Larsen [5]. For a π-wall the exact solutions reveal that the central 'core' of the wall will always move radially towards the centre of the sample while the domain wall half-width (half of the 'annular width' of the wall) will change as the core of the wall propagates, depending on the magnitude of the field and the sign of the magnetic anisotropy. The approximating nonlinear equations will also be solved numerically for two different $\frac{\pi}{2}$-walls in section 3.3. For $\frac{\pi}{2}$-walls the core of the wall may propagate radially inwards or outwards and this will depend on the imposed boundary conditions, the magnitude of the field and the sign of the magnetic anisotropy. Many of the features that will appear in the solutions displayed below share similarities to the effects that have been discussed for nematic liquid crystals using radially comoving coordinates [4]. The paper concludes with a discussion of the results in section 4.

2. Geometrical set-up and governing equation

In this section we introduce the mathematical description of the problem and derive the governing dynamic equation. The mathematical model for a general radial domain wall will be given in section 2.1. The relevant dynamic theory is presented in section 2.2, which then leads to the key governing dynamic equation (2.40) for radial domain walls that is derived in section 2.3. The solutions to this equation for various boundary conditions will be the focus of our attention in section 3 and the remainder of the paper.

2.1. Geometrical set-up

Consider a film of planar aligned SmC liquid crystal in which the smectic layer normal **a** is parallel to the z-axis as shown in figure 2(a), where only one representative smectic layer is shown schematically in cross-section for emphasis (there are, of course, many more parallel layers stacked upon each other). Boundary conditions at planes where z is constant are neglected; the sample depth in the z-direction can be assumed thin (e.g., a freely suspended film) or have any thickness with appropriate boundary conditions. It is the radial domain wall in the xy-plane that is the key phenomenon to be investigated. A long straight wire carrying a current I is modelled by a solid circular cylinder of radius r_0 placed along the z-axis. It is well known from the Biot and Savart law [12, section 5.2] that, under idealized conditions, this current will induce a circular magnetic field **B**, known as the magnetic induction: the lines of magnetic induction form concentric circles around the wire, as indicated in figure 2. Figure 2(a) shows a cross-section through the xz-plane of a single SmC layer which lies in the xy-plane and gives an indication of the anticipated alignment of the director **n** as viewed along the y-direction, represented by the short bold lines. Competing boundary conditions on the director at the central cylindrical boundary and radially far from the centre of the sample will induce a radial domain wall across which the alignment of the director changes from one constant state to another. This wall will be located over the grey annular region shown in figure 2(b), where the 'core' of the wall (where the orientation angle of the director is precisely mid-way between the two competing boundary states) is represented by the dashed circle located at the time-dependent distance $\rho(t)$ from the origin in the xy-plane. The time-dependent annular region will propagate radially and the radial depth of the annular region

itself will also expand or contract under the influence of the magnetic field, depending upon the material properties of the liquid crystal.

Figure 2(*b*) introduces the geometry used for the mathematical description of the domain wall. As in Stelzer and Arodź [4], it is advantageous to work with the comoving coordinate frame described in figure 2(*b*). The coordinate ξ is introduced as a measure of the *outwards* radial distance from $\rho(t)$. Thus the 'outer' and 'inner' edges of the wall are located at $\rho(t)+\xi_0(t)$ and $\rho(t)-\xi_1(t)$, respectively, where $\xi_0(t)$ is the time-dependent radial distance from the core of the wall to the outer edge and $\xi_1(t)$ is the distance from the core to the inner edge, as shown in the figure. The usual polar angle α is also introduced. Thus the comoving coordinate system has coordinates ξ, α and z with basis vectors $\widehat{\boldsymbol{\xi}}$, $\widehat{\boldsymbol{\alpha}}$ and $\widehat{\mathbf{z}}$, respectively. These basis vectors can be found via their connection to Cartesian coordinates through the relations

$$x=(\rho(t)+\xi)\cos\alpha, \qquad y=(\rho(t)+\xi)\sin\alpha, \qquad z=z, \tag{2.1}$$

from which the usual scale factors can be derived, namely,

$$h_1=1, \qquad h_2=\rho(t)+\xi, \qquad h_3=1. \tag{2.2}$$

In the geometry of figure 2(*b*), the layer normal $\mathbf{a}$ and vector $\mathbf{c}$ may take the forms

$$\mathbf{a}=\widehat{\mathbf{z}}, \qquad \mathbf{c}=\widehat{\boldsymbol{\xi}}\sin\phi+\widehat{\boldsymbol{\alpha}}\cos\phi, \qquad \text{where} \qquad \phi=\phi(\xi,t). \tag{2.3}$$

The magnetic field for the set-up being considered here may be written as

$$\mathbf{B}=\frac{\mu_0}{2\pi}\frac{I}{\rho(t)+\xi}\widehat{\boldsymbol{\alpha}}, \tag{2.4}$$

where μ_0 is the permeability of free space. Analogous to the situation described for nematics by Stelzer and Arodź [4], it will be supposed that the director is fixed at the solid inner circular boundary and far away in the radial direction so that $\phi=\phi_1$ at r_0 and $\phi=\phi_0$ at $r=\infty$. It follows that for the domain wall introduced here we require

$$\phi(\xi,t)\equiv\begin{cases}\phi_1 & \text{between } r_0 \text{ and the inner edge of the wall,}\\ \frac{1}{2}(\phi_0+\phi_1) & \text{at the core of the wall,}\\ \phi_0 & \text{radially outwards from the outer edge of the wall.}\end{cases} \tag{2.5}$$

Between the outer and inner edges of the wall the vector $\mathbf{c}$ rotates through an angle of magnitude $|\phi_1-\phi_0|$ radians. The wall width is defined to be $\xi_0(t)+\xi_1(t)$, which is the radial distance over which $\mathbf{c}$ rotates through $|\phi_1-\phi_0|$ radians, represented by the radial depth of the grey annular region in the figure. However, it will turn out to be more convenient to work with the wall half-width $w_0(t)$ in this geometry, defined by

$$w_0(t)=\tfrac{1}{2}\left[\xi_0(t)+\xi_1(t)\right]. \tag{2.6}$$

For the comoving coordinates introduced above, the outer and inner edges of the wall are located at $\xi=\xi_0(t)$ and $\xi=-\xi_1(t)$, respectively, measured relative to the (positive) radial direction $\widehat{\boldsymbol{\xi}}$, recalling that ξ is measured from the position of $\rho(t)$.

The gradient operator in the above system of comoving cylindrical coordinates is given by

$$\nabla=\widehat{\boldsymbol{\xi}}\frac{\partial}{\partial\xi}+\widehat{\boldsymbol{\alpha}}\frac{1}{\rho(t)+\xi}\frac{\partial}{\partial\alpha}+\widehat{\mathbf{z}}\frac{\partial}{\partial z}. \tag{2.7}$$

The material time derivative with respect to the comoving frame described in the comoving coordinates is given by (see [13, p 28] for a related Cartesian form)

$$\frac{\mathrm{D}}{\mathrm{D}t}=\frac{\partial}{\partial t}+\mathbf{v}\cdot\nabla-\frac{\mathrm{d}\mathbf{r}}{\mathrm{d}t}\cdot\nabla, \tag{2.8}$$

where $\mathbf{r}(t)$ is the time-dependent position vector of the origin of the comoving frame relative to the fixed Cartesian origin and $\mathbf{v}$ is the velocity of a material element, both of these quantities being expressed in terms of the comoving coordinates. In the above set-up, $\mathbf{r}(t) = \rho(t)\widehat{\boldsymbol{\xi}}$ and it will be assumed that hydrodynamic flow will be negligible. It then follows from the usual rules for gradient operators [14] that we can write, under these particular conditions,

$$\frac{\mathrm{D}}{\mathrm{D}t} = \frac{\partial}{\partial t} - \frac{\mathrm{d}\rho}{\mathrm{d}t}\frac{\partial}{\partial \xi}, \tag{2.9}$$

as noted by Stelzer and Arodź [4]. This operator is actually applicable to both scalars and vectors because of the particular form for $\mathbf{r}(t)$ adopted here.

2.2. *SmC continuum theory*

Here we briefly present the relevant parts of the SmC dynamic continuum theory introduced by Leslie *et al* [15] for isothermal incompressible SmC liquid crystals; a summary and a review of some general developments of this theory may be found in [3]. We shall adopt Cartesian index notation as appropriate where repeated indices are summed from 1 to 3. The vectors $\mathbf{a}$ and $\mathbf{c}$ are subject to the constraints

$$\mathbf{a}\cdot\mathbf{a} = 1, \qquad \mathbf{c}\cdot\mathbf{c} = 1, \qquad \mathbf{a}\cdot\mathbf{c} = 0, \qquad \nabla\times\mathbf{a} = \mathbf{0}. \tag{2.10}$$

The dynamic equations arising from the balance of linear momentum may be neglected in the present problem because flow is assumed negligible. This is quite common practice in liquid crystal theory [3, p 315] and it also happens to be the position adopted by Stelzer and Arodź [4] for nematics. The remaining governing dynamic equations are those that arise from the balance of angular momentum. They consist of the two coupled sets of equations

$$\left(\frac{\partial w}{\partial a_{i,j}}\right)_{,j} - \frac{\partial w}{\partial a_i} + G_i^a + \tilde{g}_i^a + \gamma a_i + \mu c_i + \epsilon_{ijk}\beta_{k,j} = 0, \tag{2.11}$$

$$\left(\frac{\partial w}{\partial c_{i,j}}\right)_{,j} - \frac{\partial w}{\partial c_i} + G_i^c + \tilde{g}_i^c + \kappa c_i + \mu a_i = 0, \tag{2.12}$$

where w is the SmC elastic energy density and $i = 1, 2$ or 3. The scalar functions γ, μ and κ and the vector function $\boldsymbol{\beta}$ are Lagrange multipliers that arise from the constraints (2.10). Equations (2.11) and (2.12) are often referred to as the a-equations and c-equations, respectively. In these equations the generalized external body forces per unit volume related to $\mathbf{a}$ and $\mathbf{c}$ are denoted by $\mathbf{G}^a$ and $\mathbf{G}^c$, respectively. Although there is no fluid flow, there will be time-dependent effects related to the orientation of the director. Such effects occur due to the presence of the dynamic terms $\tilde{g}_i^a$ and $\tilde{g}_i^c$ which, in the absence of flow, are given by

$$\tilde{g}_i^a = -2\left(\lambda_4\dot{a}_i + \lambda_6 c_i c_p \dot{a}_p + \tau_5\dot{c}_i\right), \tag{2.13}$$

$$\tilde{g}_i^c = -2\left(\lambda_5\dot{c}_i + \tau_5\dot{a}_i\right), \tag{2.14}$$

where $\lambda_4, \lambda_5, \lambda_6$ and τ_5 are dynamic viscosity coefficients and a superposed dot represents the usual material time derivative (the full forms for these terms when flow is present may be found in [3, 15]). It often proves convenient to introduce the notation

$$\Pi_i^a = \left(\frac{\partial w}{\partial a_{i,j}}\right)_{,j} - \frac{\partial w}{\partial a_i}, \qquad \Pi_i^c = \left(\frac{\partial w}{\partial c_{i,j}}\right)_{,j} - \frac{\partial w}{\partial c_i}. \tag{2.15}$$

Further details of this particular SmC dynamic continuum theory, and a brief discussion on the viscosity coefficients and the physical significance of the Lagrange multipliers, may be

found in [3]. The a- and c-equations are the relevant dynamic equations for what we consider here; it is shown below that the a-equations will be satisfied automatically by a judicious choice of Lagrange multipliers (essentially because the layers are assumed fixed in space) so that it is really the c-equations that will be of significance.

There are a number of equivalent ways of writing the elastic energy density for SmC [16]. The one that proves convenient here may be written as [3, 15, 16]

$$\begin{aligned} w = {} & \tfrac{1}{2}K_1(\nabla\cdot\mathbf{a})^2 + \tfrac{1}{2}K_2(\nabla\cdot\mathbf{c})^2 + \tfrac{1}{2}K_3(\mathbf{a}\cdot\nabla\times\mathbf{c})^2 + \tfrac{1}{2}K_4(\mathbf{c}\cdot\nabla\times\mathbf{c})^2 \\ & + \tfrac{1}{2}K_5(\mathbf{b}\cdot\nabla\times\mathbf{c})^2 + K_6(\nabla\cdot\mathbf{a})(\mathbf{b}\cdot\nabla\times\mathbf{c}) + K_7(\mathbf{a}\cdot\nabla\times\mathbf{c})(\mathbf{c}\cdot\nabla\times\mathbf{c}) \\ & + K_8(\nabla\cdot\mathbf{c})(\mathbf{b}\cdot\nabla\times\mathbf{c}) + K_9(\nabla\cdot\mathbf{a})(\nabla\cdot\mathbf{c}), \end{aligned} \tag{2.16}$$

where K_i, $i = 1, 2, \ldots, 9$ are elastic constants and the vector $\mathbf{b} = \mathbf{a}\times\mathbf{c}$ has been introduced for ease of notation. The magnetic energy potential for general liquid crystals, in terms of the magnetic induction $\mathbf{B}$, is the negative of the usual magnetic energy density and is given by [3, p 30]

$$\Psi_{\mathrm{m}} = \tfrac{1}{2}\mu_0^{-1}\Delta\chi\,(\mathbf{n}\cdot\mathbf{B})^2, \tag{2.17}$$

where $\Delta\chi$ is the unitless magnetic anisotropy, which may be positive or negative for different materials. The related generalized body forces then take the forms [3, p 263]

$$G_i^a = \mu_0^{-1}\Delta\chi\,(\mathbf{n}\cdot\mathbf{B})B_i\cos\theta, \qquad G_i^c = \mu_0^{-1}\Delta\chi\,(\mathbf{n}\cdot\mathbf{B})B_i\sin\theta, \tag{2.18}$$

where, as mentioned earlier, $\mathbf{n} = \mathbf{a}\cos\theta + \mathbf{c}\sin\theta$. The results quoted here are valid provided the magnetic susceptibilities are small [17], an assumption that has been found generally acceptable in many liquid crystal applications.

2.3. Governing dynamic equations

We now derive the governing equations to be discussed in this paper using the theory outlined in the previous section. Constraints (2.10) are satisfied for the forms of $\mathbf{a}$ and $\mathbf{c}$ stated at equation (2.3). Calculations reveal that

$$\nabla\cdot\mathbf{a} = 0, \tag{2.19}$$

$$\nabla\cdot\mathbf{c} = \frac{1}{(\rho(t)+\xi)}\frac{\partial}{\partial\xi}\left[(\rho(t)+\xi)\sin\phi\right], \tag{2.20}$$

$$\nabla\times\mathbf{c} = \frac{1}{(\rho(t)+\xi)}\frac{\partial}{\partial\xi}\left[(\rho(t)+\xi)\cos\phi\right]\widehat{\mathbf{z}}, \tag{2.21}$$

$$\mathbf{a}\cdot\nabla\times\mathbf{c} = \frac{1}{(\rho(t)+\xi)}\frac{\partial}{\partial\xi}\left[(\rho(t)+\xi)\cos\phi\right], \tag{2.22}$$

$$\mathbf{c}\cdot\nabla\times\mathbf{c} = 0, \tag{2.23}$$

$$\mathbf{b}\cdot\nabla\times\mathbf{c} = 0. \tag{2.24}$$

Further, using standard results from [18] that involve the scale factors (2.2), it is found that (see [3, p 265] for general vector expressions for Π^a and Π^c which considerably reduce the standard calculations)

$$\Pi^a = -K_3(\mathbf{a}\cdot\nabla\times\mathbf{c})(\nabla\times\mathbf{c}) - K_8(\nabla\cdot\mathbf{c})(\mathbf{c}\times\nabla\times\mathbf{c}) + K_9\nabla(\nabla\cdot\mathbf{c}), \tag{2.25}$$

$$\begin{aligned} \Pi^c = {} & K_2\nabla(\nabla\cdot\mathbf{c}) - K_3\nabla\times\{(\mathbf{a}\cdot\nabla\times\mathbf{c})\mathbf{a}\} \\ & - K_7\left[\nabla\times\{(\mathbf{a}\cdot\nabla\times\mathbf{c})\mathbf{c}\} + (\mathbf{a}\cdot\nabla\times\mathbf{c})(\nabla\times\mathbf{c})\right] - K_8\nabla\times\{(\nabla\cdot\mathbf{c})\mathbf{b}\}. \end{aligned} \tag{2.26}$$

Note that the contributions involving K_7 and K_8 in Π^c have components in the $\widehat{\mathbf{z}}$ direction only. Equations (2.4) and (2.18) lead to

$$\mathbf{G}^a = B(\xi,t)\sin\theta\cos\theta\widehat{\alpha}, \qquad \mathbf{G}^c = B(\xi,t)\sin^2\theta\widehat{\alpha}, \tag{2.27}$$

where

$$B(\xi,t) = \frac{\mu_0\Delta\chi}{4\pi^2}\frac{I^2}{(\rho(t)+\xi)^2}\cos\phi. \tag{2.28}$$

It also follows from the material derivative defined in equation (2.9) and expressions (2.13) and (2.14) that

$$\tilde{\mathbf{g}}^a = -2\tau_5\dot{\mathbf{c}}, \qquad \tilde{\mathbf{g}}^c = -2\lambda_5\dot{\mathbf{c}}, \tag{2.29}$$

where

$$\dot{\mathbf{c}} = \cos\phi\left(\frac{\partial\phi}{\partial t} - \frac{\mathrm{d}\rho}{\mathrm{d}t}\frac{\partial\phi}{\partial\xi}\right)\widehat{\boldsymbol{\xi}} - \sin\phi\left(\frac{\partial\phi}{\partial t} - \frac{\mathrm{d}\rho}{\mathrm{d}t}\frac{\partial\phi}{\partial\xi}\right)\widehat{\alpha}. \tag{2.30}$$

We now deal with the a-equations and c-equations separately.

2.3.1. The a-equations. To solve the a-equations (2.11) it is sufficient to identify the Lagrange multipliers γ, μ and $\boldsymbol{\beta}$. We follow the general procedure outlined by Stewart *et al* [19] that was based on an extension to curvilinear coordinates of a general procedure for Cartesian coordinates: see [20, section 67] and [3, p 304]. The multiplier μ can be determined by taking the scalar product of the c-equations (2.12) with $\mathbf{a} = \widehat{\mathbf{z}}$ and using the results from (2.26), (2.27), (2.29) and (2.30) to find that

$$\mu(\xi,t) = -\Pi_3^c. \tag{2.31}$$

It is well known that for any differentiable vector $\boldsymbol{\mathcal{F}}$,

$$\nabla\cdot\boldsymbol{\mathcal{F}} = \mathbf{0} \qquad \text{if and only if} \qquad \boldsymbol{\mathcal{F}} = \nabla\times\boldsymbol{\mathcal{G}}, \tag{2.32}$$

for some twice differentiable vector $\boldsymbol{\mathcal{G}}$, called the vector potential, which is unique apart from the addition of the gradient of an arbitrary scalar field. Since $\nabla\cdot(\nabla\times\boldsymbol{\beta}) = 0$, the divergence of the a-equations in (2.11) can be taken to eliminate $\boldsymbol{\beta}$, leaving a differential equation for the scalar function multiplier γ. If we set the left-hand side of the a-equations to be in the form $\boldsymbol{\mathcal{F}} + \nabla\times\boldsymbol{\beta}$, then taking the divergence of both sides of equation (2.11) gives $\nabla\cdot\boldsymbol{\mathcal{F}} = 0$, which gives the differential equation to solve for γ. Once a solution for γ has been identified, the result in equation (2.32) can be applied to conclude that there exists a unique (apart from the gradient of a scalar field) differentiable vector field $\boldsymbol{\mathcal{G}}$ which satisfies $\boldsymbol{\mathcal{F}} = \nabla\times\boldsymbol{\mathcal{G}}$. We can then set $\boldsymbol{\beta} = -\boldsymbol{\mathcal{G}}$. It then follows that $\boldsymbol{\mathcal{F}} + \nabla\times\boldsymbol{\beta} = \mathbf{0}$, so that the a-equations (2.11) are satisfied: the solution for γ guarantees the existence of $\boldsymbol{\beta}$ and the consequent fulfilment of the a-equations. Knowledge that the differential equation for γ has a solution is therefore sufficient to guarantee the existence of the vector multiplier $\boldsymbol{\beta}$, which does not need to be calculated explicitly (unless it is specifically required). It is known [3, 21] that if a particular type of smectic layer configuration is supposed then the vector $\boldsymbol{\beta}$ can provide a mechanism through the couple stress to transmit the torques needed to maintain the assumed layer configuration. The divergence of (2.11) in the comoving coordinates, using (2.25), (2.27), (2.29) and (2.30), leads to the differential equation

$$\frac{1}{\rho(t)+\xi}\frac{\partial}{\partial\xi}\left[(\rho(t)+\xi)\left(\Pi_1^a + \tilde{g}_1^a + \mu c_1\right)\right] + \frac{\partial\gamma}{\partial z} = 0. \tag{2.33}$$

This can clearly be integrated to find that

$$\gamma(\xi,\alpha,z,t) = -\frac{z}{\rho(t)+\xi}\frac{\partial}{\partial\xi}\left[(\rho(t)+\xi)\left(\Pi_1^a + \tilde{g}_1^a + \mu c_1\right)\right] + M(\xi,\alpha,t), \tag{2.34}$$

where M is an arbitrary function of ξ, α and t. It follows that, provided $\rho(t)+\xi$ is never zero and that a solution for $\phi(\xi,t)$ can be found from the c-equations, γ can be determined from (2.34), thereby guaranteeing the existence of a vector multiplier $\boldsymbol{\beta}$ so that the a-equations are satisfied. It may be of interest to note that in this instance we can find $\boldsymbol{\beta}$ explicitly. It is given by

$$\beta_1 = (\rho(t)+\xi)\int^{\alpha} M(\xi,\widetilde{\alpha},t)\,\mathrm{d}\widetilde{\alpha} + \frac{\partial Y}{\partial \xi}, \tag{2.35}$$

$$\beta_2 = -\frac{1}{\rho(t)+\xi}\left\{\int^{\xi}(\rho(t)+\widetilde{\xi})\Pi_3^a(\widetilde{\xi},t)\,\mathrm{d}\widetilde{\xi} - z(\rho(t)+\xi)\left(\Pi_1^a+\tilde{g}_1^a+\mu c_1\right) - \frac{\partial Y}{\partial \alpha}\right\}, \tag{2.36}$$

$$\beta_3 = \int^{\xi}\left(\Pi_2^a(\widetilde{\xi},t)+G_2^a(\widetilde{\xi},t)+\tilde{g}_2^a(\widetilde{\xi},t)+\mu(\widetilde{\xi},t)c_2(\widetilde{\xi},t)\right)\mathrm{d}\widetilde{\xi} + \frac{\partial Y}{\partial z}, \tag{2.37}$$

where Y is an arbitrary differentiable function of ξ, α, z and t. It can be verified directly via (2.3), (2.27), (2.29), (2.30) and the results in (2.34)–(2.37) that $\boldsymbol{\beta}$ satisfies the a-equations (2.11) because

$$\nabla\times\boldsymbol{\beta} = -(\Pi_1^a+\tilde{g}_1^a+\mu c_1)\widehat{\boldsymbol{\xi}} - \left(\Pi_2^a+G_2^a+\tilde{g}_2^a+\mu c_2\right)\widehat{\boldsymbol{\alpha}} - \left(\Pi_3^a+\gamma\right)\widehat{\mathbf{z}}. \tag{2.38}$$

This fortunate position has chiefly arisen because it has been assumed that there is no flow and that the layer normal **a** remains fixed; in general, if **a** is non-constant then it will be non-trivial to solve the a-equations coupled to the c-equations. Thus it only remains to determine and solve the c-equations in order to find complete solutions to all the relevant equations.

2.3.2. The c-equations. The Lagrange multiplier μ, which couples the a-equations to the c-equations, has been identified at equation (2.31). The remaining multiplier κ may be found by taking the scalar product of the c-equations with **c**. Alternatively, κ may be eliminated from the c-equations as follows, noting that for $i=3$ the corresponding equation in (2.12) is automatically satisfied by the insertion of μ derived above so that only the first and second of the c-equations remain. We can multiply the first equation by c_2 and the second by c_1 and then subtract them. This eliminates κ and produces the final governing dynamic equation, namely,

$$\Pi_1^c c_2 - \Pi_2^c c_1 + \tilde{g}_1^c c_2 - \tilde{g}_2^c c_1 - G_2^c c_1 = 0. \tag{2.39}$$

Recall that contributions related to K_7 and K_8 do not appear in Π_1^c and Π_2^c, as noted after (2.26). A straightforward insertion of the expressions in equations (2.3), (2.20), (2.22), (2.26)–(2.30) into (2.39) delivers the key dynamic equation for the problem discussed here. This governing dynamic equation for $\phi(\xi,t)$ is therefore

$$\begin{aligned}2\lambda_5\left[\frac{\partial\phi}{\partial t}-\frac{d\rho}{\mathrm{d}t}\frac{\partial\phi}{\partial\xi}\right] &= K_2\cos\phi\frac{\partial}{\partial\xi}\left[\frac{1}{(\rho(t)+\xi)}\frac{\partial}{\partial\xi}\left[(\rho(t)+\xi)\sin\phi\right]\right]\\ &\quad -K_3\sin\phi\frac{\partial}{\partial\xi}\left[\frac{1}{(\rho(t)+\xi)}\frac{\partial}{\partial\xi}\left[(\rho(t)+\xi)\cos\phi\right]\right]\\ &\quad -\frac{\mu_0\Delta\chi}{4\pi^2}\frac{I^2\sin^2\theta}{(\rho(t)+\xi)^2}\sin\phi\cos\phi.\end{aligned} \tag{2.40}$$

It is known [15] that $\lambda_5>0$ while the elastic constants K_2 and K_3, which are equivalent to the constants B_2 and B_1, respectively, introduced by the Orsay Group [22], are positive [15, 3]. Equation (2.40) forms the basis for the work in this paper. Its solution will require solutions for both $\rho(t)$ and $\phi(\xi,t)$ in order to determine the complete dynamics of the director.

3. Solutions for ρ and ϕ

3.1. Polynomial approximation and boundary conditions

The nonlinear equation (2.40) has no known exact solutions and is similar in structure to the various cases discussed by Stelzer and Arodż [4] for nematics. We shall construct an approximating system of coupled nonlinear equations that can be solved analytically in special cases by adopting a method of polynomial expansion that has been developed for such problems by Arodż [9, 10], Stelzer and Arodż [4], Arodż and Stelzer [11] and Arodż and Larsen [5].

The main idea is to take the spatial dependence of $\phi(\xi, t)$ as a Taylor-like expansion with respect to the wall distance ξ around the 'core' value at $\xi = 0$, that is, around $\phi(0, t)$. From figure 2 and equation (2.5) it is seen that

$$\phi(0, t) = \tfrac{1}{2}(\phi_0 + \phi_1) \qquad \text{for all} \qquad t \geqslant 0. \tag{3.1}$$

A Taylor expansion around $\xi = 0$ to third order in ξ then allows a polynomial approximation for $\phi(\xi, t)$ to be made with time-dependent coefficients of the form

$$\phi(\xi, t) = \tfrac{1}{2}(\phi_0 + \phi_1) + a(t)\xi + \tfrac{1}{2}b(t)\xi^2 + \tfrac{1}{6}c(t)\xi^3. \tag{3.2}$$

From the description in section 2.1, the instantaneous wall width is given by $2w_0 = \xi_0(t) + \xi_1(t)$. From figure 2 and (2.5) the boundary conditions are (recall that ξ is measured relative to the position of the core at $\rho(t)$)

$$\phi(\xi_0, t) = \phi_0, \qquad \phi(-\xi_1, t) = \phi_1, \tag{3.3}$$

$$\frac{\partial}{\partial\xi}\phi(\xi_0, t) = 0, \qquad \frac{\partial}{\partial\xi}\phi(-\xi_1, t) = 0. \tag{3.4}$$

The boundary conditions stated at (3.4) ensure smoothness of the solution for ϕ at the edges of the annular region. Substituting the above boundary conditions into the polynomial approximation (3.2) for ϕ leads to the relations

$$a\xi_0 + \tfrac{1}{2}b\xi_0^2 + \tfrac{1}{6}c\xi_0^3 = \tfrac{1}{2}(\phi_0 - \phi_1), \tag{3.5}$$

$$a\xi_1 - \tfrac{1}{2}b\xi_1^2 + \tfrac{1}{6}c\xi_1^3 = \tfrac{1}{2}(\phi_0 - \phi_1), \tag{3.6}$$

$$a + b\xi_0 + \tfrac{1}{2}c\xi_0^2 = 0, \tag{3.7}$$

$$a - b\xi_1 + \tfrac{1}{2}c\xi_1^2 = 0. \tag{3.8}$$

These equations form a set of inhomogeneous linear equations for the time-dependent coefficients a, b and c. Using Gaussian elimination, it is seen that for consistency, with ξ_0 and ξ_1 both non-zero, we require

$$\xi_0(t) = \xi_1(t), \qquad b = 0, \tag{3.9}$$

which means that the partial wall widths ξ_0 and ξ_1 must be identical, showing that the wall half-width $w_0 = \xi_0(t)$, and that there are no quadratic terms in ξ in the approximation for ϕ. This results in

$$a = -\frac{\xi_0^2}{2}c = \frac{3}{4}\frac{(\phi_0 - \phi_1)}{\xi_0}, \tag{3.10}$$

$$c = -\frac{3}{2}\frac{(\phi_0 - \phi_1)}{\xi_0^3}. \tag{3.11}$$

Further, it is possible to use (3.10) to express c in terms of a as

$$c = -\frac{3}{2}\frac{(\phi_0 - \phi_1)}{\xi_0^3} = -\frac{32}{9}\frac{1}{(\phi_0 - \phi_1)^2}a^3. \tag{3.12}$$

The results in (3.10)–(3.12) show that the coefficients in the cubic expansion of ϕ can all be expressed in terms of $a(t)$ (or $\xi_0(t)$) and the constants ϕ_0 and ϕ_1. We choose to work with $a(t)$ for convenience in the calculations below: a straightforward conversion to the more physically relevant wall half-width $w_0 = \xi_0(t)$ will be made as required via (3.10).

We can now insert a, b and c into the polynomial expansion (3.1) to give ϕ in terms of $a(t)$, ϕ_0 and ϕ_1. The trigonometric terms in the dynamic equation (2.40) are then expanded up to third order in ξ. The corresponding coefficients of the powers of ξ that appear in the fully differentiated version of (2.40) are then equated to zero to obtain approximating dynamic equations. As highlighted in previous work [4], meaningful results can be obtained by inspecting the nonlinear equations that arise from the zeroth and first orders in ξ only (note that to do this we must take ϕ to at least third order in ξ because of the second derivatives that occur in (2.40)). The two equations from the zeroth and first order are, respectively,

$$\begin{aligned} 2\lambda_5\frac{\mathrm{d}\rho}{\mathrm{d}t} &= (K_2 - K_3)\left[\frac{1}{2}\left(a + \frac{1}{a\rho^2}\right)\sin(\phi_0 + \phi_1) - \frac{1}{\rho}\cos^2((\phi_0 + \phi_1)/2)\right] \\ &\quad - K_3\frac{1}{\rho} + \frac{\mu_0\Delta\chi}{8\pi^2 a}\frac{I^2}{\rho^2}\sin^2\theta\sin(\phi_0 + \phi_1), \end{aligned} \tag{3.13}$$

$$\begin{aligned} 2\lambda_5\frac{\mathrm{d}a}{\mathrm{d}t} &= (K_2 - K_3)\left[\left(\frac{1}{\rho^3} - \frac{a^2}{\rho}\right)\sin(\phi_0 + \phi_1) - \left(a^3 + \frac{a}{\rho^2}\right)\cos(\phi_0 + \phi_1)\right. \\ &\quad \left. - \left(\frac{a}{\rho^2} + \frac{32}{9}\frac{a^3}{(\phi_0 - \phi_1)^2}\right)\cos^2((\phi_0 + \phi_1)/2)\right] - K_3\left[\frac{a}{\rho^2} + \frac{32}{9}\frac{a^3}{(\phi_0 - \phi_1)^2}\right] \\ &\quad - \frac{\mu_0\Delta\chi}{4\pi^2}\frac{I^2}{\rho^3}\sin^2\theta\left[a\rho\cos(\phi_0 + \phi_1) - \sin(\phi_0 + \phi_1)\right]. \end{aligned} \tag{3.14}$$

We shall suppose that initial conditions are supplied at $t = 0$ so that

$$\rho(0) = \rho_0, \qquad a(0) = a_0, \tag{3.15}$$

the latter condition leading to an initial condition for ξ_0 given via (3.10) as

$$\xi_0(0) = \frac{3}{4}\frac{(\phi_0 - \phi_1)}{a_0}. \tag{3.16}$$

Solutions to the above equations for $\rho(t)$ and $\xi_0(t)$ (determined from $a(t)$ via relation (3.10)) now form the basis of the remainder of the work in this paper. We note that at any given instant the solution $\phi(\xi, t)$ is given via (3.2), (3.9) and (3.12) by

$$\phi(\xi, t) = \begin{cases} \phi_1, & \text{for} \quad r_0 \leqslant \xi \leqslant -\xi_0(t), \\ \dfrac{1}{2}(\phi_0 + \phi_1) + a(t)\xi - \dfrac{16}{27}\dfrac{1}{(\phi_0 - \phi_1)^2}a^3(t)\xi^3, & \text{for} \quad -\xi_0(t) < \xi < \xi_0(t), \\ \phi_0, & \text{for} \quad \xi \geqslant \xi_0(t). \end{cases} \tag{3.17}$$

In general, numerical solutions to the coupled nonlinear differential equations (3.13) and (3.14) have to be sought. Nevertheless, in the special case of a π-wall the exact solutions for ρ and a can be determined because equation (3.13) decouples from (3.14), as will now be demonstrated. These exact solutions provide a particularly clear insight into the behaviour of the more general cases that can be generated numerically.

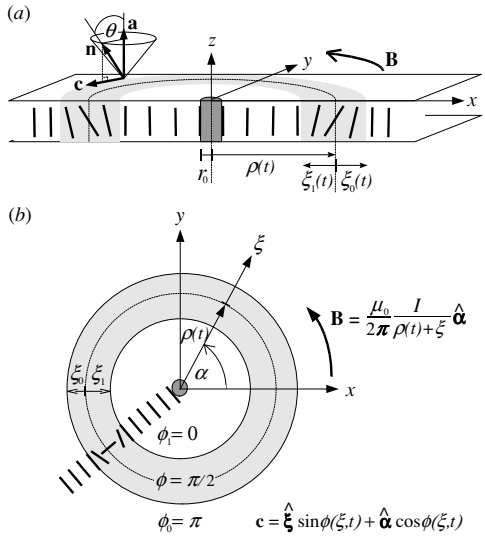

Figure 3. (*a*) Cross-section, similar to that in figure 2(*a*), with bold lines indicating the alignment of the director for a π-wall as seen by an observer looking along the y-axis with $\phi = \frac{\pi}{2}$ at the core of the domain wall. At $\xi_0(t)$ the alignment of **a**, **c** and **n** are as shown, where $\phi_0 = \pi$ and $\mathbf{c} = \widehat{\alpha}$. (*b*) The wall as seen by an observer looking down the z-axis. The bold lines here represent schematically a typical radially dependent alignment of the vector **c** within the xy-plane as it reorients through π radians across the wall: the full alignment consists of many such 'spokes'. The annular wall width will expand or contract and the core will move radially inwards or outwards as the wall adjusts to the effects of the magnetic induction **B** and the competition between constant states.

3.2. The π-wall

In this section we investigated the special case of a π-wall where we can set $\phi_0 = \pi$ and $\phi_1 = 0$ with $\phi = \frac{\pi}{2}$ at the core of the wall, as shown in figure 3. The core is located at $\rho(t)$, measured as shown in figure 3(*a*), and it is known from (3.9) that $\xi_0(t) = \xi_1(t)$ and that the wall half-width is then $w_0(t) = \xi_0(t)$. The short bold lines in figure 3(*b*) represent the alignment of **c** as seen by an observer looking down the z-axis and focussing on one representational radial element; this pictured dependence of **c** on the radial coordinate is assumed uniform in the α- and z-directions. Inserting $\phi_0 = \pi$ and $\phi_1 = 0$ into equation (3.13) gives

$$\frac{\mathrm{d}\rho}{\mathrm{d}t} = -\frac{K_3}{2\lambda_5\rho}, \tag{3.18}$$

which can be solved exactly to find

$$\rho(t) = \rho_0\,(1 - \beta t)^{\frac{1}{2}}\,, \tag{3.19}$$

where

$$\beta = \frac{K_3}{\lambda_5\rho_0^2}. \tag{3.20}$$

This indicates that the core of the wall will move radially inwards and that this solution for ρ is valid for $0 \leqslant t < t_\mathrm{m}$ where $t_\mathrm{m} = 1/\beta$ is the maximum time for which $\rho(t)$ is valid. Clearly, $\mathrm{d}\rho/\,\mathrm{d}t$ diverges and ρ tends to zero as $t \to t_\mathrm{m}$; however, physically, this situation cannot occur because of the presence of the solid central cylinder of radius r_0. The result for ρ can

be inserted into equation (3.14) to find that the nonlinear differential equation for $a(t)$ is then given by

$$\frac{\mathrm{d}a}{\mathrm{d}t} = \frac{\beta\delta}{2(1-\beta t)}a - Na^3, \tag{3.21}$$

where, for ease of notation,

$$\delta = \frac{1}{K_3}\left(K_2 - 2K_3 + \frac{\mu_0\Delta\chi}{4\pi^2}I^2\sin^2\theta\right), \tag{3.22}$$

$$N = \frac{1}{2\lambda_5}\left(K_3 - K_2 + \frac{32}{9}\frac{K_3}{\pi^2}\right). \tag{3.23}$$

We remark here that an interchange in the roles of ϕ_0 and ϕ_1 in this particular example does not alter the differential equations (3.18) and (3.21), as can be checked by direct substitution into equations (3.13) and (3.14) while exercising care in the calculation for $a(t)$, which, from its definition in (3.10), changes sign when the roles of ϕ_0 and ϕ_1 are reversed: this invariance is not generally true, as will be seen in the following section for $\frac{\pi}{2}$-walls. The dimensionless quantity δ is a measure of the magnitude of the current in relation to the elastic constants and it may be negative or positive, depending upon the magnitude of I and the sign of the (dimensionless) magnetic anisotropy $\Delta\chi$. Both δ and N also depend upon the anisotropy of the elastic constants. Equation (3.21) is a Bernoulli-type equation and therefore we can make the substitution

$$a(t) = 1/\sqrt{v(t)}, \tag{3.24}$$

to obtain a linear differential equation in v. The resulting equation is

$$\frac{\mathrm{d}v}{\mathrm{d}t} + \frac{\beta\delta}{(1-\beta t)}v = 2N. \tag{3.25}$$

An integrating factor for this equation is $(1-\beta t)^{-\delta}$ and, after some straightforward integration, this leads to the solution, for $v(0) = v_0$,

$$v(t) = \begin{cases} \dfrac{2N}{\beta(1-\delta)}[(1-\beta t)^{\delta} - (1-\beta t)] + v_0(1-\beta t)^{\delta}, & \text{for} \quad \delta \neq 1, \\ -2\dfrac{N}{\beta}(1-\beta t)\ln(1-\beta t) + v_0(1-\beta t), & \text{for} \quad \delta = 1, \end{cases} \tag{3.26}$$

valid for $0 \leqslant t < 1/\beta$. For $v(t)$ to remain positive for arbitrary positive v_0 and for all δ we require that $N > 0$. This leads to a restriction in the relative values of the elastic constants, namely,

$$K_2 < K_3\left(1 + \frac{32}{9\pi^2}\right). \tag{3.27}$$

We remark here that the elastic constants K_2 and K_3 are not those for nematics. Nevertheless, they are expected to be of a similar magnitude to the well-known nematic elastic constants and whether or not the inequality (3.27) is generally satisfied remains to be determined for SmC materials: it has been established experimentally [23] that $K_2 < K_3$ for most nematic liquid crystals. If $N < 0$ then the differential equation (3.21) will have real solutions, but their existence will depend, unlike the solution in (3.26), on the relative magnitudes of β, δ and the arbitrary positive initial data $v_0 = a_0^2$.

Under the assumption that $N > 0$, the solution $a(t)$ is easily obtained from (3.24) and (3.26) while the more physically relevant solution for the wall half-width $\xi_0(t)$ is given via $a(t)$ through relation (3.10), which shows that

$$\xi_0(t) = \begin{cases} \left\{ \dfrac{9\pi^2 N}{8\beta(1-\delta)}[(1-\beta t)^{\delta} - (1-\beta t)] + \xi_0^2(0)(1-\beta t)^{\delta} \right\}^{\frac{1}{2}}, & \text{for} \quad \delta \neq 1, \\ \left\{ -\dfrac{9\pi^2 N}{8\beta}(1-\beta t)\ln(1-\beta t) + \xi_0^2(0)(1-\beta t) \right\}^{\frac{1}{2}}, & \text{for} \quad \delta = 1. \end{cases} \tag{3.28}$$

Note that $\xi_0(t)$ is continuous with respect to δ at $\delta = 1$, as can be seen by taking the appropriate limit $\delta \to 1$ in (3.28). The solutions $\rho(t)$ and $\xi_0(t)$ are the key solutions to our problem since ρ tracks the position of the core of the domain wall while ξ_0 gives the half-width of the domain wall, which is represented by half of the radial depth of the annular region pictured in figure 3. The solution for $\phi(\xi, t)$ is given via (3.17), (3.24), (3.26) and (3.28) by

$$\phi(\xi, t) = \begin{cases} 0, & \text{for} \quad r_0 \leqslant \xi \leqslant -\xi_0(t), \\ \dfrac{\pi}{2} + a(t)\xi - \dfrac{16}{27\pi^2}a^3(t)\xi^3, & \text{for} \quad -\xi_0(t) < \xi < \xi_0(t), \\ \pi, & \text{for} \quad \xi \geqslant \xi_0(t). \end{cases} \tag{3.29}$$

The solution to the problem for a π-wall is therefore completely encapsulated by the explicitly available solutions for $\rho(t)$, $\xi_0(t)$ and $\phi(\xi, t)$ given by (3.19), (3.28) and (3.29), respectively.

It is seen from (3.28) that as $t \to t_{\mathrm{m}} \equiv 1/\beta$,

$$\xi_0(t) \to \begin{cases} 0, & \text{for} \quad \delta > 0, \\ \sqrt{\dfrac{9\pi^2}{8\beta}N + \xi_0^2(0)}, & \text{for} \quad \delta = 0, \\ \infty, & \text{for} \quad \delta < 0, \end{cases} \tag{3.30}$$

noting, as above, that $N > 0$ is required for the solution ξ_0 to be valid for arbitrary initial data. From the experimental set-up described above, t will never actually approach t_{m} because $\rho(t) - \xi_0(t)$ will equal the inner solid circular radius r_0 at some time τ at which both the core radius ρ and the growth or expansion of the annular region halt (recall that $\xi_0(t) = \xi_1(t)$ by (3.9)). Therefore the value of τ must lie within the time interval $[0, t_{\mathrm{m}})$ and

$$\rho(\tau) - \xi_0(\tau) = r_0. \tag{3.31}$$

This means that the extreme situation in equation (3.30) will not occur and therefore $\phi(\xi, t)$ will always be valid as a solution for $0 \leqslant t \leqslant \tau$, with $-\xi_0(t) \leqslant \xi \leqslant \xi_0(t)$.

We shall look at some particular solutions for positive and negative values of δ for a set of typical material parameters and select, when required, suitable data from the following list, which is based upon typical nematic parameters [3]:

$$K_2 = 3.8 \times 10^{-12}\ \mathrm{N}, \qquad K_3 = 7.5 \times 10^{-12}\ \mathrm{N}, \qquad \mu_0 = 4\pi \times 10^{-7}\ \mathrm{H\,m^{-1}},$$
$$\Delta\chi = 1.2 \times 10^{-6}, \qquad \theta = \frac{\pi}{6}, \qquad \lambda_5 = 3 \times 10^{-2}\ \mathrm{Pa\,s}. \tag{3.32}$$

The effect of anisotropy in the elastic constants K_2 and K_3 is evident in the explicit solution for $\xi_0(t)$ via the constants N and δ, bearing in mind our requirement that N be positive, and we therefore concentrate on the behaviour of solutions as δ varies or changes sign. For an inner cylindrical core and initial conditions, examples will use

$$r_0 = 2.5 \times 10^{-4}\ \mathrm{m}, \qquad \rho(0) = 3.5 \times 10^{-4}\ \mathrm{m}, \qquad \xi_0(0) = 10^{-6}\ \mathrm{m}. \tag{3.33}$$

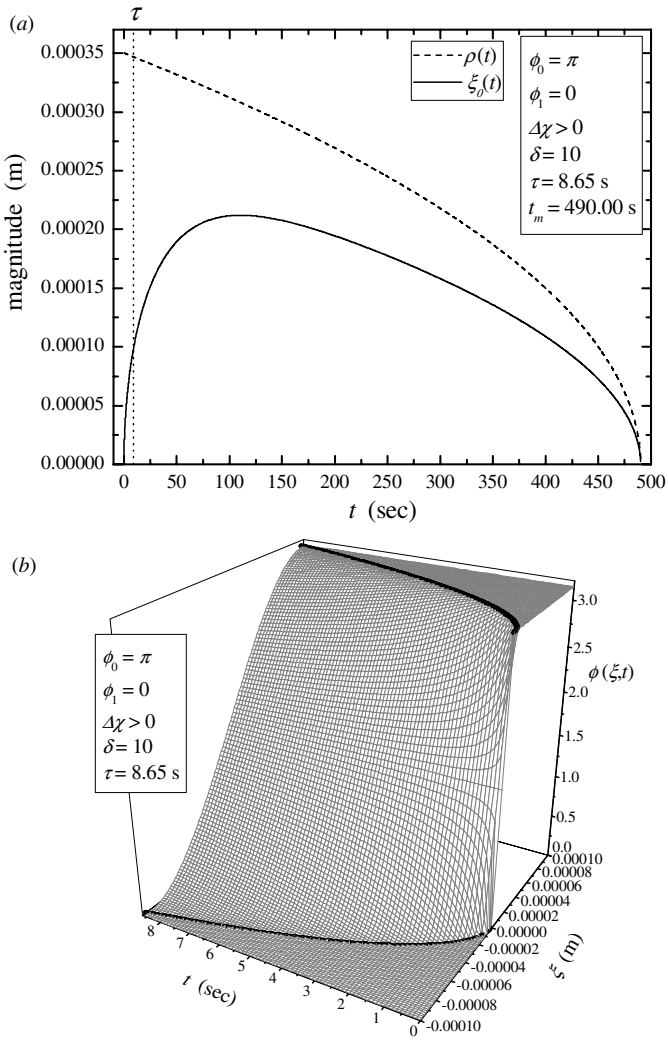

Figure 4. (*a*) The solutions (3.19) and (3.28) for the location $\rho(t)$ of the core of the wall and the wall half-width $\xi_0(t)$, respectively, for a π-wall. The material parameters used in calculations are as stated in (3.32) and (3.33); the dimensionless parameter δ, defined in (3.22), depends upon the magnitude of the current I and has been set to 10 as an illustration. The dynamics of the wall will cease at time $t = \tau$ despite the solutions being available up to the maximum time $t_{\rm m}$, for reasons that are explained in the text. (*b*) The evolution of the orientation angle $\phi(\xi, t)$ of **c** for the solutions calculated in (*a*) over the interval $0 \leqslant t \leqslant \tau$, obtained from the results in (3.24), (3.26), (3.28) and (3.29). The bold curves correspond to the time dependence of the inner and outer edges of the domain wall for $0 \leqslant t \leqslant \tau$: the upper bold curve coincides with the curve for $\xi_0(t)$ in (*a*) when placed in the plane $\phi \equiv \pi$, while the lower curve is obtained by symmetry, as detailed in the text.

The solutions for $\rho(t)$, $\xi_0(t)$ and $\phi(\xi, t)$ are shown in figure 4 for the material parameters (3.32) and conditions (3.33) when $\delta = 10$. The full solutions for $0 \leqslant t \leqslant t_{\rm m}$, where $t_{\rm m}$ has been calculated as 490 s, are shown in figure 4(*a*) where it is seen that ρ decreases monotonically to zero while the expansion of the wall half-width ξ_0 reaches a maximum before decreasing to zero, in accordance with the general result (3.30) for positive values of δ. The calculated time

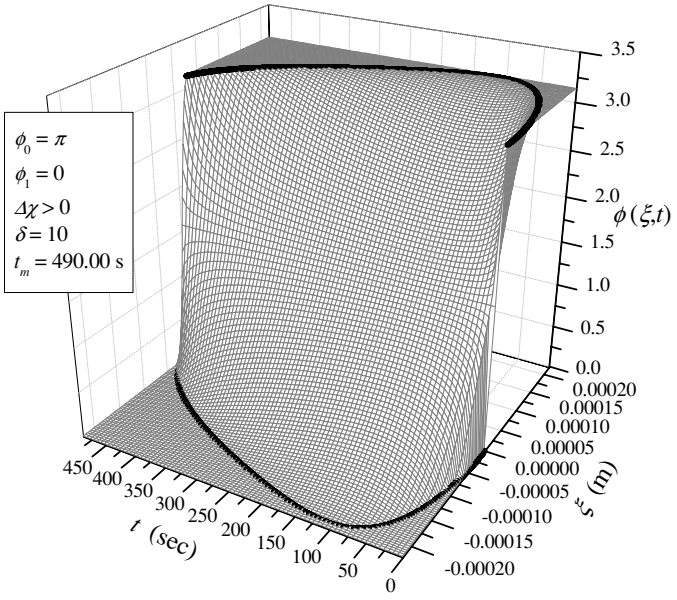

Figure 5. The π-wall solution for $\phi(\xi, t)$ over the time interval $0 \leqslant t \leqslant t_{\rm m}$: other details are identical to those for figure 4. Figure 4(b) is a restriction of this solution to $0 \leqslant t \leqslant \tau$, as discussed in the text.

at which the growth of ξ_0 and the reduction in ρ cease, i.e. when relation (3.31) is satisfied, is $\tau = 8.65$ s, which is below $t_{\rm m}$. For any experimental set-up with a non-zero central cylinder of radius $r_0 > 0$ both the reduction of ρ towards the origin and the expansion or contraction of ξ_0 will halt at some value τ with $0 \leqslant \tau \leqslant t_{\rm m}$, as indicated earlier. An increase in r_0 will shift τ closer to zero while a decrease in r_0 will shift τ towards $t_{\rm m}$. This can be seen from the vertical distance between $\rho(t)$ and $\xi_0(t)$ in figure 4(a): the length of the dotted vertical line at $t = \tau$ between $\rho(t)$ and $\xi_0(t)$ is equal to r_0. Figure 4(b) shows the solution (3.29) for $\phi(\xi, t)$ for $0 \leqslant t \leqslant \tau$, obtained via the results in equations (3.24), (3.26), (3.28) and (3.29). The bold curves represent the time evolution of the wall boundaries at $\pm\xi_0(t)$. The plane $\xi = 0$ is, of course, located at $\rho(t)$ and the displayed behaviour of ϕ is therefore relative to the moving coordinates frame. The upper bold curve lying in the ξt-plane coincides with the curve for $\xi_0(t)$ in figure 4(a) on the interval $0 \leqslant t \leqslant \tau$ when it is placed in the plane $\phi \equiv \pi$ while the lower bold curve is obtained by symmetry around the $\xi = 0$ plane since the outer wall-width $\xi_0(t)$ is equal to the inner wall-width $\xi_1(t)$, by (3.9). Figure 5 shows the general evolution of $\phi(\xi, t)$ for $0 \leqslant t \leqslant t_{\rm m}$ and is displayed for information so that the profile for ϕ can be anticipated for different values of τ (which have to be calculated for different values of r_0). The relevant solution for ϕ is that portion of the surface generated over the interval $0 \leqslant t \leqslant \tau$: see figure 4($b$), which is the relevant part of the surface in figure 5.

Graphs for other positive values of δ produce qualitatively similar results. Nevertheless, for high values of δ (which correspond to fields of large magnitude) a metastable state in $\xi_0(t)$ appears, analogous to some of the special cases for nematics discussed by Stelzer and Arodź [4]. For $\delta = 600$, $t_{\rm m} = 490$ s, $\tau = 188.8$ s and the value of $\xi(t)$ is almost constant for a period of time after an initial increase, as can be seen in figure 6(a) and its inset for small times relative to $t_{\rm m}$. Eventually, the full solution for the wall half-width ξ_0 decreases to zero. As before, the dynamics will cease at $t = \tau$ when relation (3.31) is fulfilled, as marked in

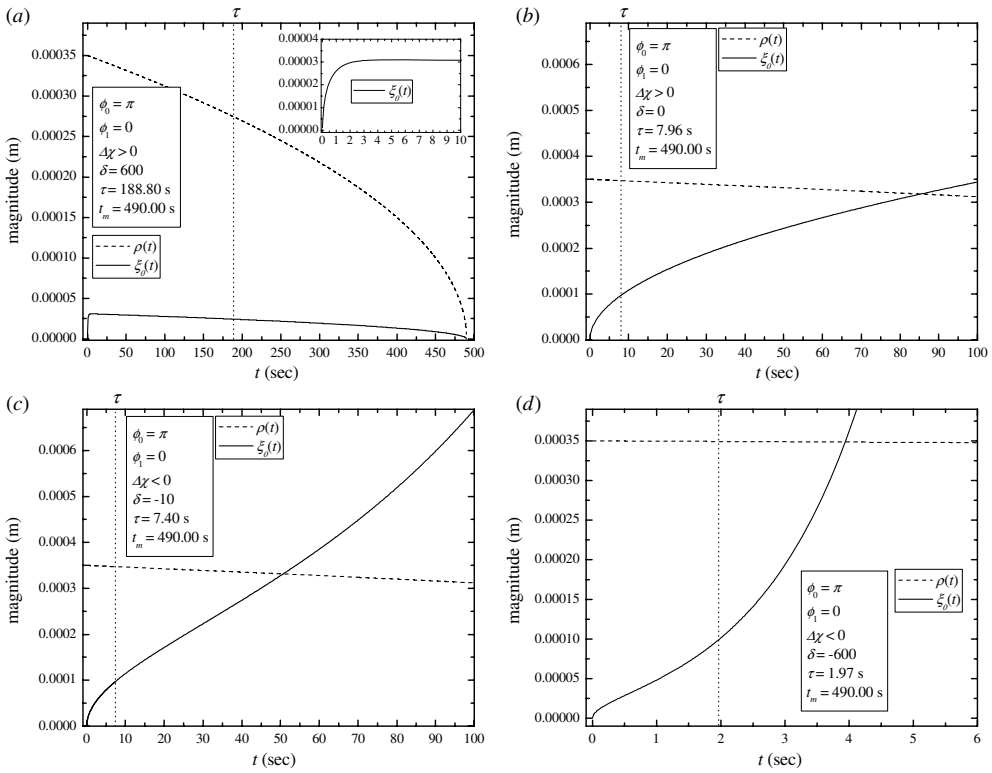

Figure 6. (*a*) An example for a π-wall with high magnitude field. The material parameters are as stated in (3.32) and (3.33), as for figures 4 and 5, except that here $\delta = 600$. For small times relative to t_m a metastable state appears for ξ_0 as shown in the inset, analogous to the situation for a related nematic problem discussed in [4]. The dynamics will cease at $t = \tau$ when relation (3.31) is satisfied. (*b*) The π-wall for $\delta = 0$, the remaining parameters as for (*a*). The solutions $\rho(t)$ and $\xi_0(t)$ coincide at a time t_c where $\tau < t_c < t_m$. The dynamics will always cease at $t = \tau$ before these solutions can coincide, due to the presence of the solid wire in the region $0 \leqslant r \leqslant r_0$. (*c*) and (*d*) The π-wall for $\Delta\chi = -1.2 \times 10^{-6}$ and $\delta = -10$ (*c*) and $\delta = -600$ (*d*). The results in (*c*) and (*d*) are qualitatively similar to those in (*b*) except that τ has decreased with decreasing δ.

figure 6(*a*). It is noted that the time τ has increased from that obtained for $\delta = 10$ while t_m must remain the same.

Although most materials have $\Delta\chi > 0$, for completeness we consider briefly the case for $\Delta\chi < 0$. It is perhaps first worth noting that, for the material values stated in (3.32), $\delta = -1.49$ when $I = 0$; for $\delta < -1.49$ we require $\Delta\chi < 0$. As examples for negative magnetic anisotropy we have examined solutions for $\delta = -10$ and $\delta = -600$ and replaced the magnetic anisotropy by $\Delta\chi = -1.2 \times 10^{-6}$, the other material parameters and conditions in (3.32) and (3.33) remaining unchanged. The results are shown in figures 6(*c*) and (*d*) where the values for τ have been calculated numerically. As predicted by the result in (3.30) for $\delta < 0$, $\xi_0(t)$ increases to infinity as $t \to t_m$ while $\rho(t)$ remains as above, given by (3.19), and decreases to zero at $t = t_m$. The behaviour is essentially qualitatively similar to the $\delta > 0$ case, in that a time τ can be calculated, as indicated in the figure, at which the decrease in ρ and increase in ξ_0 stop because their difference equals r_0, at which time relation (3.31) holds, as before. The corresponding solutions for $\phi(\xi, t)$ for $0 \leqslant t \leqslant \tau$ will be similar in appearance to those shown in figures 4 and 5. One apparent difference is that no metastable behaviour

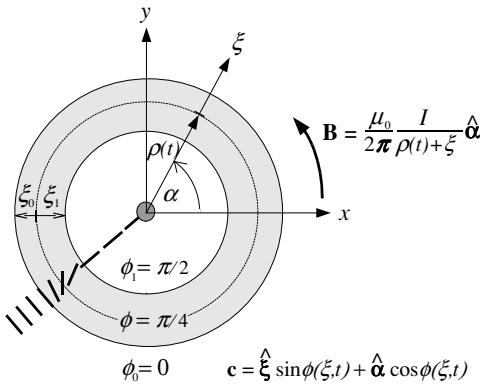

Figure 7. A $\frac{\pi}{2}$-wall when $\phi_0 = 0, \phi_1 = \frac{\pi}{2}$ and $\phi = \frac{\pi}{4}$ at the core of the domain wall. The alignment of the vector **c** is indicated schematically by the short bold lines placed along the radial direction. Other general details are as mentioned in figure 2.

in $\xi_0(t)$ seems to occur for large negative values of δ, in contrast to that for large positive values of δ. Another key difference for $\delta < 0$ is that there will always a critical time t_c, with $\tau < t_c < t_m$, at which $\rho(t_c) = \xi_0(t_c)$, as can be seen from figures 6(*c*) and (*d*): the dynamic process will cease before $t = t_c$ because $r_0 > 0$, due to the presence of the solid wire in the region $0 \leqslant r \leqslant r_0$. Further, the solutions cannot make physical sense for $t > t_c$ because $\rho(t)$ cannot actually be less than the half wall-width $\xi_0(t)$. Qualitatively similar results have been obtained for other negative values of δ. Note also that τ decreased from $\tau = 7.40$ s to $\tau = 1.79$ s as δ decreased from $\delta = -10$ to $\delta = -600$.

Given the behaviour stated at (3.30) for $\xi_0(t)$ as $t \to t_m$, one particularly special case of interest is the solution for $\delta = 0$. The results are presented in figure 6(*b*) using the parameters from (3.32) and (3.33). As above, $\rho(t)$ will be unchanged for these values: however, in this case, setting $\delta = 0$ is equivalent to selecting a current I such that δ is zero. In this example, $I \approx 34.25$ A. The solutions are similar to those in figures 6(*c*) and (*d*) in that times τ and t_c, $\tau < t_c < t_m$, with the same features as before, can be calculated. The earlier comments concerning such times τ and t_c are equally valid here also.

3.3. $\pi/2$-walls

As mentioned previously, numerical solutions to equations (3.13), (3.14) and (3.15) need to be generated for general values of ϕ_0 and ϕ_1 because, unlike the special case of a π-wall, the nonlinear differential equations do not decouple. Recall that $\xi_0(t)$ is obtained from the solution for $a(t)$ via relation (3.10). Two different $\frac{\pi}{2}$-walls will now be investigated. For brevity, we shall only consider the case for $\Delta\chi > 0$. Other walls for $\Delta\chi < 0$ and different values of ϕ_0 and ϕ_1 may be generated by similar procedures.

The first $\frac{\pi}{2}$-wall to be considered is when $\phi_0 = 0$ and $\phi_1 = \frac{\pi}{2}$, as pictured in figure 7 where a typical view of the alignment of the vector **c** is shown by the short bold lines located along the radial direction. Other details of the wall are the same as those in figure 2. The solutions for $\rho(t)$ and $\xi_0(t)$ are displayed in figure 8(*a*) for the same material parameters stated at equations (3.32) and (3.33) used for the π-wall (with $\Delta\chi > 0$). The parameter δ is no longer available explicitly and so, as an illustrative example, the current has been set as $I = 1$ A. As before, there is a time τ at which relation (3.31) will hold and the dynamics of the wall will stop. The inset graph in figure 8(*a*) shows the time evolution of $\rho(t)$ and $\xi_0(t)$

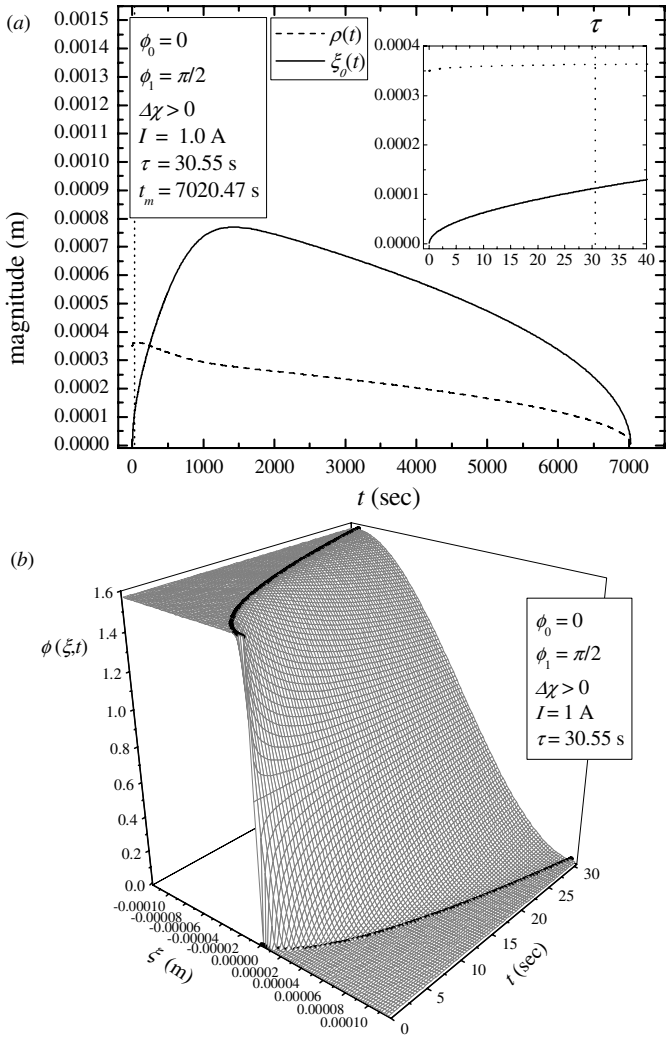

Figure 8. (*a*) Solutions for $\rho(t)$ and $\xi_0(t)$ calculated numerically from equations (3.13), (3.14) and (3.15), via (3.10), for the $\frac{\pi}{2}$-wall where $\phi_0 = 0$ and $\phi_1 = \frac{\pi}{2}$. The material parameters are as stated in (3.32) and (3.33) and the current has been set to $I = 1$ A. The dynamics will stop at $t = \tau$, indicted by a vertical dotted line, as discussed in the text. The inset shows the solutions for $0 \leqslant t \leqslant \tau$. (*b*) The $\frac{\pi}{2}$-wall solution for the orientation angle $\phi(\xi, t)$ of **c** obtained from equation (3.17) and the numerical solutions for $\rho(t)$, $\xi_0(t)$ and $a(t)$. The bold curves correspond to the time dependence of the inner and outer edges of the domain wall and are derived from the solutions for $\xi_0(t)$, as detailed in the text.

up to the time τ. One striking difference with the analogous results for a π-wall in figure 6(*a*) is that the solutions for $\rho(t)$ and $\xi_0(t)$ intersect at some time t_c, with $\tau < t_c < t_m$, where t_m is the calculated maximum time for the availability of these time-dependent solutions; such behaviour only occurs for a π-wall when $\Delta\chi < 0$. For the same reasons mentioned at the end of section 3.2, the dynamics must cease before time t_c is reached, due to the presence of the solid wire in the region $0 \leqslant r \leqslant r_0$. Figure 8(*b*) shows the solution for the orientation angle $\phi(\xi, t)$ of **c** obtained from equation (3.17) and the numerical solutions for $\rho(t)$, $\xi_0(t)$ and $a(t)$ (derived from relation (3.10)). This graph is similar in form to that for the π-wall in

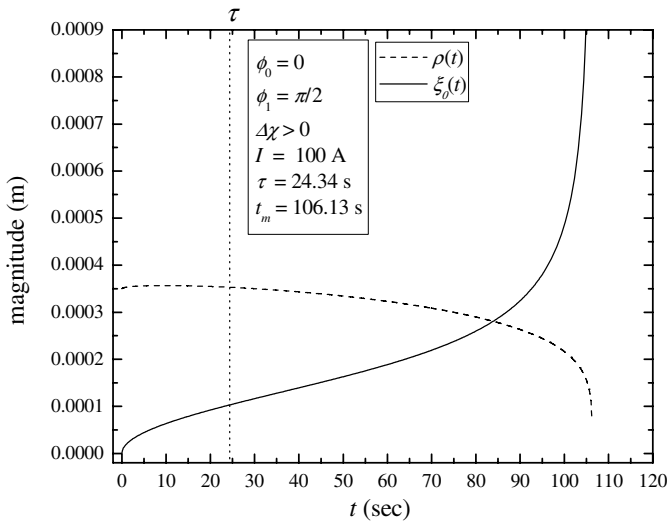

Figure 9. Solutions for $\rho(t)$ and $\xi_0(t)$ for the same parameters used in figure 8 for the $\frac{\pi}{2}$-wall with $\phi_0 = 0$ and $\phi_1 = \frac{\pi}{2}$, except that here the current has been set as $I = 100$ A to demonstrate typical behaviour for a high magnitude induced field. The solutions for $\rho(t)$ and $\xi_0(t)$ coincide a $t = t_c$ where $\tau < t_c < t_m$. The maximum time t_m for the existence of time-dependent solutions has been calculated numerically. The dynamics will always cease at $t = \tau$ before these solutions can coincide, due to the presence of the solid wire in the region $0 \leqslant r \leqslant r_0$.

figure 4(*b*) where, as before, the plane $\xi = 0$ is located at $\rho(t)$ so that the displayed behaviour of ϕ is therefore relative to the moving coordinates frame. The bold curves are analogous to those in figures 4(*b*) and 5 and correspond to the time dependence of the inner and outer edges of the domain wall for $0 \leqslant t \leqslant \tau$. For example, the lower curve coincides with that for $\xi_0(t)$ in figure 8(*a*) when placed in the plane $\phi \equiv 0$ while the upper curve is obtained by symmetry and the result expressed in (3.9) that requires $\xi_0(t) = \xi_1(t)$.

To demonstrate that other types of behaviour appear at higher magnitude fields, solutions have been generated for an extreme case where $I = 100$ A, the other material parameters remaining as above. The results for $\rho(t)$ and $\xi_0(t)$ are shown in figure 9. The graphs are qualitatively similar to those in figure 8(*a*) for $0 \leqslant t \leqslant \tau$, but have different qualities for $t > \tau$. For example, the domain wall half-width $\xi_0(t)$ diverges and $\rho(t)$ collapses to zero as t approaches t_m, where the maximum time t_m for the existence of time-dependent solutions has been calculated numerically. This behaviour of the solutions for $\Delta\chi > 0$ is similar to that presented above for the π-wall in figures 6(*c*) and (*d*) when $\Delta\chi < 0$: it is seen that there is a time t_c, with $\tau < t_c < t_m$, where $\rho(t_c) = \xi_0(t_c)$. Again, as in the case of the π-wall, the solutions will never actually coincide at t_c because the dynamics will stop at $t = \tau$, due to the physical presence of the conducting wire of radius $r_0 > 0$. The corresponding graph for $\phi(\xi, t)$ has not been plotted here for $I = 100$ A, but it can be seen that it will be similar in form to that for $I = 1$ A presented in figure 8(*b*), the main difference being that τ will have been reduced from $\tau = 30.55$ s to $\tau = 23.34$ s.

The second $\frac{\pi}{2}$-wall to be considered occurs when $\phi_0 = \frac{\pi}{2}$ and $\phi_1 = 0$, as pictured in figure 10. The material parameters are as for the previous $\frac{\pi}{2}$-wall and the numerical solutions for $\rho(t)$ and $\xi_0(t)$ are shown in figure 11(*a*) for $I = 1$ A. The maximum time for the existence of time-dependent solutions has been calculated numerically as $t_m = 303.56$s. As in figure 9, there is a time t_c at which these solutions coincide, with $\tau < t_c < t_m$, where τ, as

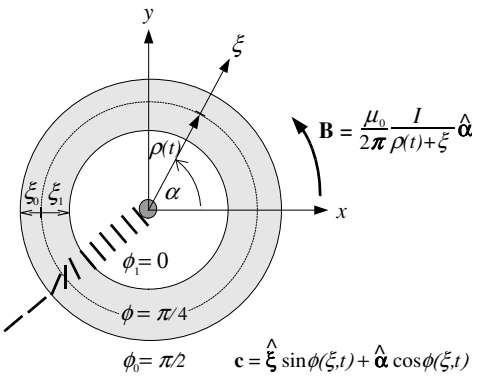

Figure 10. A $\frac{\pi}{2}$-wall when $\phi_0 = \frac{\pi}{2}, \phi_1 = 0$ and $\phi = \frac{\pi}{4}$ at the core of the domain wall. The alignment of the vector **c** is indicated schematically by the short bold lines placed along the radial direction. Other general details are as mentioned in figure 2.

before, is the time at which relation (3.31) holds. The physically relevant solutions are valid up until $t = \tau$, for the same reasons explained earlier for previous solutions. Note that, in contrast to the previous $\frac{\pi}{2}$-wall at $I = 1$ A in figure 8(*a*), $\xi_0(t)$ diverges and $\rho(t)$ collapses to zero as t approaches t_{m}. The corresponding solution for $\phi(\xi, t)$ is plotted in figure 11(*b*) and has been obtained by the same procedure used to obtain that for figure 8(*b*); the bold curves are related to the inner and outer edges of the domain wall and are to be interpreted as in previous plots for ϕ. One essential difference in this instance is that for this geometrical set-up $\tau = 17.47$ s whereas in the previous $\frac{\pi}{2}$-wall $\tau = 30.55$ s, despite all the parameters being equal apart from the interchange in the values of ϕ_0 and ϕ_1.

For further comparison with the results for the previous $\frac{\pi}{2}$-wall we also consider the case of the second $\frac{\pi}{2}$-wall for a high induced field and set $I = 100$ A, all other parameters remaining unchanged. The results are displayed in figure 12 to allow a comparison with figure 9. Similar to figure 9, there is a time τ when the domain wall dynamics cease, as indicated in the inset in figure 12. However there is one remarkable feature to the results in figure 12 that is not available in any of the previous results for domain walls. Recall that when the vertical distance between $\rho(t)$ and $\xi_0(t)$ reduces to r_0 then the wall no longer propagates, as is the case at the time τ in this example. Nevertheless, if r_0 is very small then the distance between $\rho(t)$ and $\xi_0(t)$ can never reduce to r_0 for the given initial conditions: it is easily seen from the full results in figure 12 that the location of the domain wall core at $\rho(t)$ will then always move radially outwards at a rate greater than that of the expansion in the domain wall half-width. Numerical results in this case indicate existence of solutions for all times $t \geqslant 0$. Consequently, the dynamics will never cease and the domain wall will always expand in width while propagating radially outwards, with the outer and inner edges of the wall always travelling away from the centre of the sample. This property of the domain wall is of course dependent upon the initial conditions and r_0 that have been set in equation (3.33). Qualitatively similar results for other initial conditions can be calculated numerically if desired.

4. Discussion

Theoretical results have been presented for the propagation of an annular domain wall within planar aligned samples of SmC liquid crystal. The mathematical model introduced and developed in section 2 for a comoving set of axes is quite general for a radial geometry and

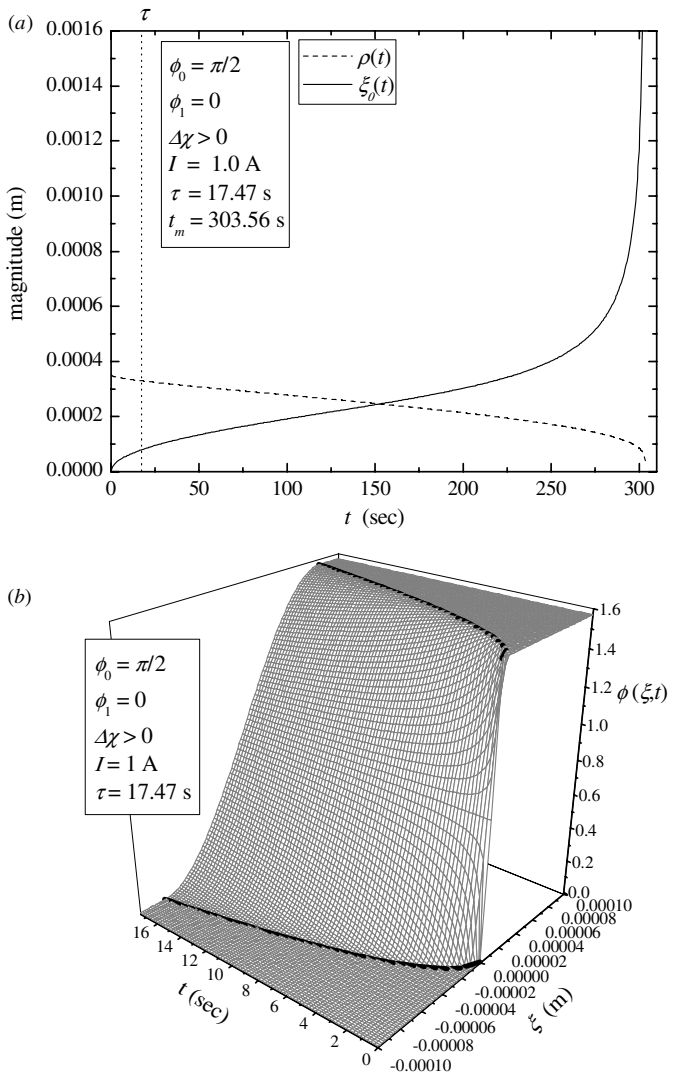

Figure 11. (*a*) Solutions for $\rho(t)$ and $\xi_0(t)$ for the $\frac{\pi}{2}$-wall when $\phi_0 = \frac{\pi}{2}$ and $\phi_1 = 0$. The remaining material parameters are the same as those used for the $\frac{\pi}{2}$-wall in figure 8 and the current has been set to $I = 1$ A. Although the solutions exist up until time $t = t_{\rm m}$ and intersect at $t_{\rm c}$, with $\tau < t_{\rm c} < t_{\rm m}$, the physically relevant solutions are only valid for $0 \leqslant t \leqslant \tau$, as discussed in the text. (*b*) The corresponding solution for $\phi(\xi, t)$ over the interval $0 \leqslant t \leqslant \tau$. The bold curves correspond to the time dependence of the inner and outer edges of the domain wall for $0 \leqslant t \leqslant \tau$, analogous to those in figure 8.

for arbitrary initial conditions which are to supplement the key governing dynamic equation (2.40) which links the location $\rho(t)$ of the moving 'core' of the domain wall and the orientation angle $\phi(\xi, t)$ of the vector **c**. In the model presented here, **c** is directly related to the alignment of the usual liquid crystal director **n** through relation (1.1) because **a** and θ are fixed (see figure 1). The domain wall occurs because of competing boundary conditions on the director at $r = r_0$ and at radially large distances far from the centre of the sample and its propagation is initiated by the presence of a conducting wire (in the region $0 \leqslant r \leqslant r_0$) that induces a circular

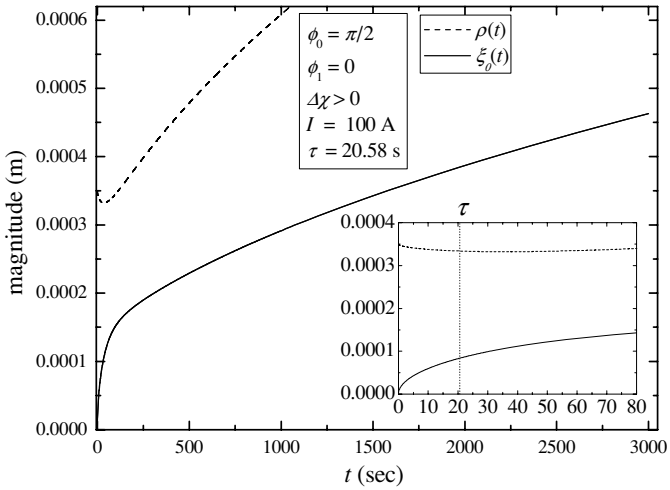

Figure 12. Solutions for $\rho(t)$ and $\xi_0(t)$ for the same parameters used in figure 9 except that the $\frac{\pi}{2}$-wall here has $\phi_0 = \frac{\pi}{2}$ and $\phi_1 = 0$; the current has been set at $I = 100$ A to demonstrate typical behaviour for a high magnitude induced field. There is a time τ at which the domain wall no longer propagates because $\rho(\tau) - \xi_0(\tau) = r_0$. Nevertheless, if r_0 is sufficiently small then it is seen that the wall will always expand in width while propagating radially outwards: see the text for details.

magnetic field which influences the orientation of the director. A time-dependent reorientation of the director arises from this competition which leads to the dynamic equation (2.40). This equation is highly nonlinear and so a polynomial expansion to third order in ξ has been used to obtain more tractable nonlinear approximations (at least third order is required if we are to retain the essential features of the nonlinearities because of the second derivatives that appear). The polynomial expansion and boundary requirements that have been derived for the wall in section 3.1 lead to the coupled system of nonlinear ordinary differential equations (3.13) and (3.14) for $\rho(t)$ and the domain wall half-width $\xi_0(t)$ (related to $a(t)$ in these equations through equation (3.10)), with $\phi(\xi, t)$ being given by (3.17).

Section 3.2 considered the particularly fortuitous special case of a π-wall, with $\phi_0 = \pi$ and $\phi_1 = 0$, where exact solutions to the nonlinear approximating equations were found for $\rho(t), \xi_0(t)$ and $\phi(\xi, t)$, given by (3.19), (3.28) and (3.29), respectively. It was noted that interchanging the roles of ϕ_0 and ϕ_1 did not alter the differential equations in this special case. The solutions are characterized by the constants β, N and the dimensionless parameter δ, defined in section 3.2. The positivity of N was a necessary condition to ensure real-valued solutions and this led to the restriction (3.27) on the relative magnitudes of the elastic constants. The parameter δ is essentially a control parameter that is a measure of the influence of the magnitude of the applied current, the magnetic anisotropy and the elastic constants. The exact solutions have been generated for the material parameters (3.32) and initial conditions (3.33) and have been plotted in figures 4, 5 and 6(a) for examples of positive magnetic anisotropy, figure 6(b) in the special case of $\delta = 0$, and in figures 6(c) and (d) for negative magnetic anisotropy. In all cases a time τ, which depends upon the initial conditions and the selection of r_0, was identified numerically via condition (3.31); at $t = \tau$ the propagation of the wall stops and it no longer propagates for $t \geqslant \tau$: the details are contained in section 3.2. One notable feature in figure 6(a), plotted in the inset, is the appearance of a metastable-like phenomenon where, after an initial period of time, the solution for the wall half-width was nearly constant

before it eventually reduced to zero, an effect that had been observed in previous work on nematic liquid crystals by Stelzer and Arodź [4].

For any other choices of boundary conditions ϕ_0 and ϕ_1 the coupled dynamic equations for $\rho(t)$ and $\xi_0(t)$ must be solved numerically. Equations (3.13) and (3.14) contain expressions that are odd in the powers of $a(t)$ and, since $a(t)$ defined in (3.10) also depends on $\phi_0 - \phi_1$, they are therefore not invariant to an interchange in the roles of ϕ_0 and ϕ_1. This asymmetry in the dynamic equations means that, in general, the results must change when the values of ϕ_0 and ϕ_1 are interchanged. Further, since explicit exact solutions are generally unavailable, a restriction on the relative magnitudes of the elastic constants, analogous to that in (3.27), is no longer explicitly available and the occurrence of any such restriction would have to be investigated numerically. As typical examples we considered two particular $\frac{\pi}{2}$-walls in section 3.3. The results are presented in figures 8 and 9 for $\phi_0 = 0$ and $\phi_1 = \frac{\pi}{2}$, and in figures 11 and 12 for $\phi_0 = \frac{\pi}{2}$ and $\phi_1 = 0$, using the same set of material parameters as those used for the π-wall for $\Delta\chi > 0$. With the exception of the high magnitude current case in figure 12, all the results are qualitatively similar to the previous cases in that a time τ can be identified at which time the wall no longer propagates. The exceptional case in figure 12 for a large current shows the remarkable property, when r_0 is sufficiently small, of a domain wall that is always increasing in width and continues to propagate radially outwards for all $t > 0$. In this case, the whole domain wall itself always travels further away from the centre of the sample because its central core travels further in the radially outwards direction than its expansion in wall half-width, so that the dynamics will continue and there will be no time τ at which it will halt. We have been dealing with radially infinite samples in this paper and, of course, from physical considerations such a wall will actually cease propagating when the distance $\rho(t) + \xi_0(t)$ equals that measured radially from $r = 0$ to a boundary surface, that is, it may continue to expand until its 'outer' domain wall edge located at $\rho(t) + \xi_0$ reaches the outer extremities of the sample. The numerical results for the $\frac{\pi}{2}$-walls share many of the features that have been discovered for the exact solutions related to the π-wall, one important difference being the aforementioned possibility of a propagating wall possessing the growth qualities that appear in figure 12.

A fascinating aspect of the work presented here is the insight to the possibility of a π-wall 'collapse' at the origin at a critical time when $\rho(t) = \xi_0(t) = 0$, which could only happen if no wire were present at the origin: see figures 4(*a*) and 6(*a*). For the π-wall introduced above this would mean that the wall would vanish at $t = t_{\mathrm{m}} = 1/\beta$, which can be calculated using (3.20). If it were possible to induce an annular domain wall that propagates in the absence of any solid wire placed along the z-axis then a domain wall collapse could be envisaged for $\delta > 0$, in analogy with the catastrophic behaviour of the wall half-width for Bloch walls in nematic liquid crystals discussed by Stelzer and Arodź [4]. For a π-wall with $\delta < 0$, again in the absence of any wire, there will be a time t_{c} when $\rho(t) = \xi_0(t) \neq 0$, which differs from the case for $\delta > 0$: see figure 6. In this situation the solution for $\xi_0(t)$ (which equals that for the 'inner' wall half-width $\xi_1(t)$) does not make physical sense for $t > t_{\mathrm{c}}$ and it is not clear if the core of the wall could continue to expand outwards or not. However, these are merely speculative observations that have arisen from an inspection of the results in the figures. Similar comments apply to the results for the $\frac{\pi}{2}$-walls displayed in figures 8, 9 and 11. In figure 12 the domain wall expansion does not diverge at a finite time, as far as numerical experiments have indicated. This expansion is perhaps in contrast with the catastrophic behaviour in the expansion of the wall half-width encountered for times close to a finite critical time for a Néel wall in nematics discussed by Stelzer and Arodź [4], the difference here being that the solutions appear to exist for all positive time, as far as numerical experiments have indicated.

Work that is connected to the domain walls discussed here is that concerned with the appearance of multiple ring pattern formations that can occur in samples of ferroelectric smectic C liquid crystals (SmC*) under the influence of rotating electric fields. Each circular ring that appears in such patterns may be modelled by a single radially dependent domain wall that can travel in the radial direction as time advances. Some experimental results of interest, and details of experimental set-ups, may be found in the articles by Hauck *et al* [24], Dascālu *et al* [25] and Link *et al* [26]. Some preliminary theoretical results have been obtained by Kilian *et al* [27], who have reported some analysis that involves critical electric field strengths and the velocity of the rings. Wigham and Stewart [28] have also examined the theoretical stability of some basic ring patterns in SmC* liquid crystals. A common feature shared by the results for ring patterns in SmC* with those contained in this paper for SmC is the possible propagation of a domain wall in the radial direction that is induced by the presence of an applied field. It is conceivable that multiple domain walls in SmC could occur for the experiment proposed in this paper and, in this context, the results we have presented could be considered as the dynamics of one 'ring', especially when metastable states occur such as those discussed for figure 6(*a*).

The results in this paper have been derived under the assumption that there is no flow. The incorporation of a non-zero fluid velocity will lead to a larger system of complex nonlinear dynamic equations. The possibility of finding exact solutions, even for nonlinear approximations to such equations, is limited and a more advanced numerical procedure would have to be invoked. Nevertheless, the effect of flow upon known exact solutions, such as those presented above in section 3.2 for a π-wall, may be investigated by considering the flow as a perturbation to the known time-dependent domain wall. This is a common practice in the analysis of the dynamics of the classical Freedericksz transition in liquid crystals [2, 3], when a set of linearized perturbation equations that incorporate flow may be solved analytically (or numerically) in order to gain insight into the flow properties of the original highly nonlinear problem. Although these procedures are generally used for examining the flow of perturbations to constant or time-independent states, the techniques may be extended to the dynamics presented here for the π-wall, especially since the exact solutions for $\rho(t)$ and $\xi_0(t)$ are known explicitly. This work is currently in progress.

References

[1] de Gennes P G and Prost J 1993 *The Physics of Liquid Crystals* 2nd edn (Oxford: Oxford University Press)
[2] Chandrasekhar S 1992 *Liquid Crystals* 2nd edn (Cambridge: Cambridge University Press)
[3] Stewart I W 2004 *The Static and Dynamic Continuum Theory of Liquid Crystals* (London: Taylor and Francis)
[4] Stelzer J and Arodź H 1997 *Phys. Rev.* E **56** 1784
[5] Arodź H and Larsen A L 1994 *Phys. Rev.* D **49** 4154
[6] Maclennan J E, Jiang Qi and Clark N A 1995 *Phys. Rev.* E **52** 3904
[7] Pociecha D, Gorecka E, Vaupotic N, Cepic M and Mieczkowski J 2005 *Phys. Rev. Lett.* **95** 207801
[8] Palffy-Muhoray P, Sparavigna A and Strigazzi A 1993 *Liq. Cryst.* **14** 1143
[9] Arodź H 1995 *Phys. Rev.* D **52** 1082
[10] Arodź H 1999 *Phys. Rev.* E **60** 1880
[11] Arodź H and Stelzer J 1998 *Phys. Rev.* E **57** 3007
[12] Jackson J D 1998 *Classical Electrodynamics* 3rd edn (New York: Wiley)
[13] Joseph D D 1990 *Fluid Dynamics of Viscoelastic Liquids* (New York: Springer)
[14] Malvern L E 1969 *Introduction to the Mechanics of a Continuous Medium* (Englewood Cliffs, NJ: Prentice-Hall)
[15] Leslie F M, Stewart I W and Nakagawa M 1991 *Mol. Cryst. Liq. Cryst.* **198** 443
[16] Leslie F M, Stewart I W, Carlsson T and Nakagawa M 1991 *Contin. Mech. Thermodyn.* **3** 237
[17] de Jeu W H 1990 *Physical Properties of Liquid Crystalline Materials* (New York: Gordon and Breach)
[18] Goodbody A M 1982 *Cartesian Tensors* (Chichester: Ellis Horwood)
[19] Stewart I W, Leslie F M and Nakagawa M 1994 *Q. J. Mech. Appl. Math.* **47** 511

[20] Rutherford D E 1957 *Vector Methods* 9th edn (Edinburgh: Oliver and Boyd)
[21] Leslie F M 1993 *Liq. Cryst.* **14** 121
[22] Orsay Group 1971 *Solid State Commun.* **9** 653
[23] Dunmur D A, Fukuda A and Luckhurst G R 2001 *Physical Properties of Liquid Crystals: Nematics EMIS Datareviews Series No. 25* (London: The Institution of Electrical Engineers (INSPEC))
[24] Hauck G, Koswig H D and Labes U 1993 *Liq. Cryst.* **14** 991
[25] Dascālu C, Hauck G, Koswig H D and Labes U 1996 *Liq. Cryst.* **21** 733
[26] Link D R, Radzihovsky L, Natale G, Maclennan J E, Clark N A, Walsh M, Keast S S and Neubert M E 2000 *Phys. Rev. Lett.* **84** 5772
[27] Kilian A, Koswig H D and Sonnet A 1995 *Mol. Cryst. Liq. Cryst.* **265** 321
[28] Wigham E J and Stewart I W 2005 *Mol. Cryst. Liq. Cryst.* **436** 955